Journal of Aerosol Science 115 (2018) 29–45

Contents lists available at ScienceDirect

Journal of Aerosol Science

journal homepage: www.elsevier.com/locate/jaerosci

Simulation of size-dependent aerosol deposition in a realistic model of the upper human airways

E.M.A. Frederix[a,*], A.K. Kuczaj[a,d], M. Nordlund[d], M. Bělka[c], F. Lizal[c], J. Jedelský[c], J. Elcner[c], M. Jícha[c], B.J. Geurts[a,b]

[a] Multiscale Modeling and Simulation, Faculty EEMCS, University of Twente, P.O. Box 217, 7500 AE Enschede, The Netherlands
[b] Anisotropic Turbulence, Fluid Dynamics Laboratory, Faculty of Applied Physics, Eindhoven University of Technology, P.O. Box 513, 5600 MB Eindhoven, The Netherlands
[c] Energy Institute, Faculty of Mechanical Engineering, Brno University of Technology, Technicka 2896/2 Brno 61669, Czech Republic
[d] Philip Morris International R & D, Philip Morris Products S.A. (part of Philip Morris International group of companies), Quai Jeanrenaud 5, 2000 Neuchâtel, Switzerland

ABSTRACT

An Eulerian internally mixed aerosol model is used for predictions of deposition inside a realistic cast of the human upper airways. The model, formulated in the multi-species and compressible framework, is solved using the sectional discretization of the droplet size distribution function to accurately capture size-dependent aerosol dynamics such as droplet drift, gravitational settling and diffusion. These three mechanisms are implemented in a consistent way in the model, guaranteeing that the total droplet mass as given by the droplet size distribution is always equal to the total droplet mass due to the mass concentration fields. To validate the model, we simulate monodisperse glycerol aerosol deposition inside the lung cast, for which experimental data is available. Provided that an adequate computational mesh is used and an adequate boundary treatment for the inertial deposition velocity, excellent agreement is found with the experimental data. Finally, we study the size-dependent deposition inside the lung cast for a polydisperse aerosol with droplet sizes ranging from the nanometer scale to beyond the micrometer scale. The typical 'V-shape' deposition curve is recovered. The aim of this paper is to 1) provide an overview of the Eulerian aerosol dynamics model and method, to 2) validate this method in a relevant complex lung geometry and to 3) explore the capabilities of the method by simulating polydisperse aerosol deposition.

1. Introduction

Aerosol research plays a major role in various branches of science and engineering. These branches concern environmental and atmospheric problems (weather, pollution, indoor air quality), engineering applications linked with sprays (combustion or cooling) or inhalation-related challenges (medical devices and dosimetry). Synergy of both experimental and computational approaches is required in order to foster deeper understanding of transport, evolution and dynamics of aerosols during inhalation. Clearly, experiments give insight into the physical processes and can provide essential information to build confidence in computational models. In fact, these models often need simplifications and heuristic input to become computationally feasible. It is then essential to validate computational models where possible. Conversely, with the further maturing of computational modeling, high levels of detail may be

* Corresponding author.
E-mail address: e.m.a.frederix@utwente.nl (E.M.A. Frederix).

http://dx.doi.org/10.1016/j.jaerosci.2017.10.007
Received 2 September 2016; Received in revised form 3 October 2017; Accepted 16 October 2017
Available online 18 October 2017

Nomenclature

List of abbreviations

BL	boundary layer
CFD	computational fluid dynamics
CMAG	condensation monodisperse aerosol generator
CMD	count median diameter
GDE	general dynamics equation
LSM	lagrangian sub-grid model
NO-BL	no boundary layer
RANS	reynolds averaged navier-stokes
ZGM	zero-gradient extrapolation model

List of indices

g	generation index
i	section index
j	species index
k	cast segment index
air	subscript indicating air
gly	subscript indicating glycerol

List of Greek symbols

ϕ_i	sectional number concentration flux ($1/m^2/s$)
Φ	inlet flow rate (m^3/s)
γ	density ratio (dimensionless)
κ	mixture heat conductivity ($kg\,m/s^3/K$)
μ	mixture viscosity (kg/m/s)
ρ	mixture mass density (kg/m^3)
ρ^ℓ	liquid mass density (kg/m^3)
ρ^v	vapor mass density (kg/m^3)
σ	geometric standard devition (dimensionless)
τ	droplet relaxation time (s)
$\boldsymbol{\tau}$	rate of strain tensor ($kg/m/s^2$)
μ_k	per-segment mean logarithmic deposition rate (dimensionless)
σ_k	per-segment standard deviation of the logarithmic deposition rate (dimensionless)
η_g	per-generation deposition efficiency (dimensionless)
ϵ_g	per-generation surface-averaged deposition efficiency (dimensionless)

List of special symbols

$\mathscr{J}_{M_i}$	source term for M_i ($1/m^3/s$)
$\mathscr{N}$	number of species
$\mathscr{P}$	number of sections
$\mathscr{Q}$	mass density source term ($kg/m^3/s$)
$\mathscr{R}_j$	vapor mass density source term ($kg/m^3/s$)
$\mathscr{S}_j$	liquid mass density source term ($kg/m^3/s$)

List of symbols

A_g	per-generation wall surface area (m^2)
c_p	mixture heat capacity at constant pressure ($m^2/s^2/K$)
C_k	per-segment numerical error measure (dimensionless)
d	droplet diameter (m)
$\mathbb{D}^\ell$	diffusion coefficient (m^2/s)
flux_i	sectional mass flux ($kg/m^2/s$)
$\mathbf{g}$	gravitational acceleration vector (m/s^2)
$\mathbf{I}$	identity matrix (dimensionless)
J	GDE source term ($1/m^3/s$)
M_i	mass-specific sectional droplet number concentration (kg^{-1})
n	droplet size distribution ($1/kg/m^3$)
$\mathbf{n}$	wall normal (dimensionless)
N_i	sectional droplet number concentration(m^{-3})
p	pressure ($kg/m/s^2$)
R_k	per-segment total deposition rate (μg/hr)
s	droplet mass (kg)
t	time (s)
T	temperature (K)
$\mathbf{u}$	mixture velocity (m/s)
$\mathbf{u}^\ell$	drift velocity (m/s)
$\mathbf{v}$	droplet velocity (m/s)
w_i	sectional weight (dimensionless)
$\mathbf{x}$	position (m)
y^+	wall distance measured in wall coordinates (dimensionless)
y_i	sectional interface size (kg)
Y_j	mass fraction of species j in vapor phase (dimensionless)
Z_j	mass fraction of species j in liquid phase (dimensionless)
Z	total liquid mass fraction (dimensionless)

provided more and more reliably, which would remain otherwise inaccessible via physical experiments alone. The combination of numerical and physical experiments can be used effectively to enhance our overall understanding of aerosol dynamics. In support, once a computational model is validated, it may serve in research areas and applications for which experiments are difficult or even impossible to conduct. A straightforward example concerns the modeling of aerosols flowing in the airways for which simulations support complex experiments and challenge experimental methods by giving insight into geometrical complexities of the flow in the respiratory tract. In this paper we present our unique compressible and consistent computational approach to model, simulate and validate complex flow deposition in the human airways. In addition, we directly confront computational predictions with experimental findings obtained from exactly the same lung cast geometry. In total, we establish a close agreement between experimental deposition data and results obtained with our Eulerian sectional aerosol model.

Simulations of aerosol deposition and respiratory tract flow analysis as a subject of computational investigations for medical and toxicological applications have been studied for many years (see the review by Hofmann (2011)). Various physical models were validated taking into account distinct levels of complexity and detail, starting from the basic formulation of droplet physics, through the development of the General Dynamics Equation (GDE) for the aerosol, and finally the application of this equation to more complex flows linked with numerical developments of Computational Fluid Dynamics (CFD) methods.

The overall goal of applying CFD to simulate the flow inside the respiratory tract is to compute the total, regional and local deposition dosimetry, which develops over successive breathing cycles. Wexler and Park (2008) presented a study estimating dosimetry values based on the developed models for aerosol droplets in the size range 0.01–10 μm, for a long exposure time. Li, Kleinstreuer, and Zhang (2007) simulated realistic tracheobronchial airways at transient airflow conditions at 15 and 60 L/min flow conditions. It was concluded that the local flow patterns, which influence particle deposition, are largely affected by secondary flows. Airway geometry as well as the flow rate play important roles. One of the important challenges in simulation of respiration is related to the development of appropriate and realistic physiology-based boundary conditions (Alzahrany & Banerjee, 2015).

Similar to our approach, various physical processes were taken into account in the framework presented by Mitsakou, Helmis, and Housiadas (2005). The framework was built in the Eulerian context and was compared against existing computational and experimental data. The quality of the computed deposition data for sub-micron particles strongly depends on the resolution of the boundary layer in time-dependent flow simulations. Since for complex geometries this requires considerable computational power, Lagrangian-based velocity corrections were proposed to improve the computational accuracy of deposition (Longest & Oldham, 2008). In order to incorporate aerosol physics for evolving liquid-based aerosols, Lagrangian and Eulerian models were built that incorporate vapor–liquid mass transport (Zhang, Kim, & Kleinstreuer, 2006; Zhang, Kleinstreuer, & Hyun, 2012). The effectiveness of both Eulerian and Lagrangian models is studied from the perspective of accuracy and computational cost (Worth Longest & Xi, 2007). In general, the Lagrangian approach is conceptually more transparent as large numbers of discrete particles are followed independently in the flow, obeying their own equations of motion and internal dynamics. However, this approach can quickly become computationally unfeasible for large particle densities. The Eulerian approach, assuming a continuous description of the particulate phase, is known to be computationally more attractive but the modeling of the interaction of the particulate phase and the fluid phase poses its own new challenges.

Validation of the developed computational models is crucial. Numerous works were devoted to this topic either in simplified or complex geometries (Feng & Kleinstreuer, 2014; Holbrook & Worth Longest, 2013; Krause et al., 2013; Ma et al., 2009; Varghese & Gangamma, 2009; Worth Longest & Oldham, 2006; Xi & Longest, 2009; Zhang, Kleinstreuer, & Kim, 2009; Zhang, Kleinstreuer, Kim, & Cheng, 2004). Validation of CFD models is not limited to the human respiratory tract alone, for example simulations of rat lungs, amongst others, have also been performed (Schroeter et al., 2016). The developed methods can be validated on the basis of existing experimental data, but should also be computationally verified with respect to the numerical discretization methods used to obtain the simulation data. Growing computational capabilities allow to simulate larger problems with more complete and richer physics (Feng, Kleinstreuer, Castro, & Rostami, 2016), that can also be fully resolved spatially and temporally if adequate computational resources, careful meshing of the domain and accurate methods are combined. Computational aerosol models require not only a fundamental and robust mathematical description of aerosol dynamics to be accurate. Their accuracy is equally dependent on the geometry and meshing in order to capture transient and interlinked processes (e.g., turbulence or diffusion and impaction of sub-micron particles). Frederix, Kuczaj, Nordlund, Veldman, and Geurts (2017), Frederix, Stanic, et al. (2017), Frederix, Stanic, Kuczaj, Nordlund, and Geurts (2016) presented an internally mixed sectional Eulerian aerosol model, designed to incorporate droplet inertial drift, sedimentation and Brownian motion. These three aerosol dynamics mechanisms drive droplet deposition in the airways. The size-dependence of these mechanisms is included by appropriate models and can be accurately simulated in the framework of sectional discretization of the droplet size distribution. Frederix, Kuczaj, et al. (2017) designed the model to respect the ‘consistency relation’; at both the analytical and numerical level the total droplet mass is equally reflected in the mass concentration fields as well as by the droplet size distribution. The model was applied to the simulation of deposition in bent pipes, and both the diffusional and inertial deposition regimes were identified and studied in one comprehensive model. The bent pipe geometry offers a reliable and well-understood point of reference for validation against other experimental, theoretical and numerical deposition data. However, the bent pipe case differs primarily in terms of the complexity of its geometry. The scope of this paper is to apply the internally mixed Eulerian aerosol model to a complex geometry that is a close representation of the actual geometry of the upper airways and to study the local and regional deposition patterns of aerosol droplets of different sizes. Furthermore, a special focus is set on comparing simulated regional aerosol deposition in the cast segments to experimentally obtained data measured by Nordlund et al. (2017) during steady-state conditions using a physical cast of the same geometry. The experimental data was obtained using a cast model consisting of several segments from the mouth cavity down to the seventh generation of branches of the lung, each representing distinct features of the respiratory tract, which can be measured for deposited mass. For the glycerol aerosol to which the cast is exposed, it was shown by Frederix, Kuczaj, et al. (2017) that for the relevant Reynolds and Stokes numbers both diffusional and inertial deposition is significant. It was also shown that in this intermediate deposition regime—the regime where diffusion and inertia are two effects of similar magnitude—it becomes numerically quite challenging to model deposition accurately. This makes the experimental data presented by Nordlund et al. (2017) extremely useful in validating our Eulerian aerosol model in realistic geometries, particularly in relation to capturing the near-wall behavior.

As was done by Frederix, Kuczaj et al. (2017) for the bent pipe, we simulate the aerosol transport and deposition using a number of different meshes with and without boundary layer mesh refinement. We include the ‘primary’ zero-gradient extrapolation model (ZGM) boundary treatment as well as the more elaborate Lagrangian sub-grid model (LSM) boundary treatment (see Longest & Oldham, 2008) to approximate the inertial deposition velocity at the wall. It is shown that on meshes without boundary layer refinement a significant overprediction of the deposition rate occurs. When applying the LSM boundary treatment, all meshes, both with and without near-wall refinement, are capable of producing a reliable prediction of the per-segment deposition rate in comparison with the regional experimental data. When looking more closely at the local deposition patterns within each cast segment, it is shown that for meshes without boundary layer refinement, the deposition appears very pixellated. If accurate predictions are required of deposition patterns with local length scales smaller than the typical features of the lung cast, refined mesh quality near

the wall is required.

Using the finest mesh with near-wall refinement and the LSM boundary treatment for the inertial velocity of droplets near the wall, we simulate a scenario where a uniform droplet size distribution spanning over a size range from 10 nm to 20 μm is released inside the lung cast. The deposition efficiency as a function of size is studied for each of the seven generations of the lung cast. For the largest particles enhanced deposition efficiency is shown in the throat segment of the cast, hindering these particles from penetrating the lung further. The typical 'V-shape' (Frederix, Kuczaj, et al., 2017) deposition curve is recovered, where in the left leg of this curve deposition is driven by diffusion and the right leg by inertia. Of the total deposited mass, we also show how the deposition is partitioned across the seven generations of the lung cast.

The novelty of the current paper lies in the fact that the recently published sectional aerosol model by Frederix, Kuczaj, et al. (2017) is now applied to the simulation of aerosol deposition inside a realistic complex lung cast of the upper airways. Specifically, the full aerosol size distribution can be simulated directly with the computational model. Moreover, the feasibility of employing Eulerian aerosol models to understand aerosol dynamics is established. Good agreement is found with experimental deposition data. The current paper extends earlier work of Longest and Oldham (2008) by introducing the sub-grid model for inertial particle deposition into the compressible flow model.

The outline of this paper is as follows. In Section 2 the Eulerian computational model is presented. This section forms a summary of what was presented by Frederix, Kuczaj, et al. (2017) and is included for completeness. In Section 3 we present simulations which mimic the experimental setup presented by Nordlund et al. (2017), and compare against these experimental data of regional deposition. We study various computational settings, addressing the influence on deposition of both the mesh refinement at the wall and the boundary treatment for the inertial deposition velocity. In Section 4 we simulate a large size range of droplets and study the per-generation deposition as a function of droplet size. In Section 5 we conclude the findings.

2. Computational modeling of aerosol transport and deposition

In this section we specify the mathematical model with which the dynamics of the aerosol droplets in a detailed lung cast is captured, closely following the recent work by Frederix, Kuczaj, et al. (2017). Subsequently, the sectional method to approximate the size distribution is presented and the contributions of drift and diffusion to the transport of droplets are described. Finally, we detail the computation of the rate of deposition of aerosol droplets on the lung tissue. We restrict to discussing the main aspects and refer to the work of Frederix, Kuczaj, et al. (2017) for full detail. The selected numerical methods that are employed in the simulations are discussed in the next section.

2.1. Mathematical model for aerosol dynamics

We adopt a compressible Eulerian description of multi-species aerosol and describe its state in terms of the mixture density ρ, the mixture velocity $\mathbf{u}$, its temperature T and species mass fractions in the vapor and liquid phases, Y_j and Z_j, respectively, for species $j = 1, ..., \mathscr{N}$ with $\mathscr{N}$ the number of different species. Although we work, in this paper, exclusively in the single-species setting we formulate the problem in the multi-species one, for the sake of generality. We opt for a compressible formulation as this is beneficial for obtaining general and accurate constitutive relations for the mixture's density dependence on temperature and pressure. In particular in cases of large temperature changes, density changes may become dominant. The generality offered by the compressible formulation allows for a natural extension of the model to settings in which density changes are important, e.g., see the work of Frederix, Stanic, et al. (2017).

The mixture mass density ρ and momentum $\rho\mathbf{u}$ adhere to the well-known continuity equation

$$\partial_t \rho + \nabla\cdot(\rho\mathbf{u}) = \mathscr{Q} \tag{1}$$

where $\mathscr{Q}$ is a source term associated with local appearance or removal of droplets due to drift or diffusion. Moreover, the dynamics is governed by the Navier-Stokes equations (we refer to the momentum transport equations as the 'Navier-Stokes' equations, following (Kundu & Cohen, 2008))

$$\partial_t(\rho\mathbf{u}) + \nabla\cdot(\rho\mathbf{u}\mathbf{u}) = -\nabla p - (\nabla\cdot\boldsymbol{\tau}) \tag{2}$$

with ∂_t the partial derivative with respect to time t, ∇ the derivative operator with respect to the spatial coordinates $\mathbf{x} \equiv (x_1, x_2, x_3)$, and rate of strain tensor $\boldsymbol{\tau}$, given by

$$\boldsymbol{\tau} = -\mu[\nabla\mathbf{u} + (\nabla\mathbf{u})^{\mathrm{T}}] + \frac{2}{3}\mu(\nabla\cdot\mathbf{u})\mathbf{I} \tag{3}$$

with the identity tensor $\mathbf{I}$ and molecular mixture viscosity μ. For the transport of energy we introduce the temperature equation in the following form (Bird, Stewart, & Lightfoot, 2007):

$$c_p[\partial_t(\rho T) + \nabla\cdot(\rho\mathbf{u}T)] = \nabla\cdot(\kappa\nabla T) - (\boldsymbol{\tau}\colon\nabla\mathbf{u}) + \mathrm{D}_t p \tag{4}$$

with c_p being the mixture heat capacity at constant pressure, κ the mixture heat conductivity and $\mathrm{D}_t \equiv \partial_t + \mathbf{u}\cdot\nabla$ the material derivative. This form of the energy equation is convenient as boundary conditions for temperature T can be readily implemented. Finally, the density can be computed from temperature and pressure using the underlying constitutive mixture equation of state, thereby closing the system. We adopt the form as, among others, used by Frederix, Kuczaj, et al. (2017), in which liquids are assumed to be

incompressible while vapors are assumed to adhere to the ideal gas law.

The transport equations for individual species transport is found from

$$\partial_t(\rho Y_j) + \nabla\cdot(\rho \mathbf{u} Y_j) = \mathscr{R}_j \tag{5a}$$

$$\partial_t(\rho Z_j) + \nabla\cdot(\rho \mathbf{u} Z_j) = \mathscr{S}_j \tag{5b}$$

with vapor and liquid sources $\mathscr{R}_j$ and $\mathscr{S}_j$ respectively. It is assumed that chemical reactions do not occur. Since

$$\sum_{j=1}^{\mathscr{N}} (Y_j + Z_j) = 1 \tag{6}$$

the summation of all equations in (5) is consistent with the continuity equation provided that

$$\sum_{j=1}^{\mathscr{N}} (\mathscr{R}_j + \mathscr{S}_j) = \mathscr{Q}. \tag{7}$$

The droplet size distribution adheres to its own transport equation, i.e., the GDE (Friedlander, 2000). It can be written as

$$\partial_t n(s, \mathbf{x}, t) + \nabla\cdot[\mathbf{u} n(s, \mathbf{x}, t)] = J(s, \mathbf{x}, t) \tag{8}$$

with right-hand side source term $J(s, \mathbf{x}, t)$ which may be used to represent a number of mechanisms such as growth by condensation and coagulation (Friedlander, 1983) as well as break-up and nucleation (Hounslow, Ryall, & Marshall, 1988). Moreover, contributions to droplet size transport due to diffusion and drift may also be incorporated. A precise detailing of the source term $J(s, \mathbf{x}, t)$ used in this paper is provided in Section 2.2.

From a physical point of view the droplet size distribution $n(s, \mathbf{x}, t)$ can be regarded as information about how many droplets we have of mass s at $(\mathbf{x}, t)$. From this interpretation it is then clear that $n(s, \mathbf{x}, t)$ also tells us how much total droplet mass is present in the system. On the other hand, this information is also carried by ρZ with $Z \equiv \sum_j Z_j$, which gives the total mass concentration of the droplet phase at $(\mathbf{x}, t)$. This means that $n(s, \mathbf{x}, t)$ and Z are related to each other as follows:

$$\rho Z = \int_0^\infty s n(s, \mathbf{x}, t) \mathrm{d}s \tag{9}$$

where the right-hand side of this relation represents the first moment of the size distribution. Within our model, this relation will prove to be very useful in the derivation of consistent transport equations for droplet drift, diffusion and deposition. We call this relation the aerosol *consistency relation*, representing the mutual consistency between liquid mass concentrations and the droplet size distribution.

2.2. Sectional approximation

The full size distribution $n(s, \mathbf{x}, t)$ may be approximated numerically using the *sectional method* (Gelbard, Fitzgerald, & Hoppel, 1998; Gelbard, Tambour, & Seinfeld, 1980; Kumar & Ramkrishna, 1996), also referred to as the *discrete population balance method*. We follow closely the approach taken by Kumar and Ramkrishna (1996). In the sectional formulation of the droplet size distribution $n(s, \mathbf{x}, t)$, the size domain is divided into $\mathscr{P}$ arbitrarily sized adjoining intervals. The i th section (with $i = 1, 2, \ldots, \mathscr{P}$) covers a part of the size domain bounded by $y_i \le s < y_{i+1}$ with y_i the position of the interface between the $(i-1)$ th and i th section. The droplets which reside in the i th section are assigned to a representative size s_i with $y_i \le s_i < y_{i+1}$, such that the complete size distribution is approximated by

$$n(s, \mathbf{x}, t) \approx \sum_{i=1}^{\mathscr{P}} N_i(\mathbf{x}, t) \delta(s - s_i) \tag{10}$$

with $N_i(\mathbf{x}, t) \ge 0$ the total number of droplets per unit of volume in the i th section and δ the Dirac delta function. Conversely, we can write

$$N_i(\mathbf{x}, t) = \int_{y_i}^{y_{i+1}} n(s, \mathbf{x}, t) \mathrm{d}s \tag{11}$$

from which it can be readily seen that N_i represents the zeroth moment of the size distribution function in the i th section and has units m^{-3}.

The rate at which the total amount of droplets within a section i changes can be derived from the GDE. In fact, by taking the integral over $[y_i, y_{i+1}]$ of (8) and using definition (11), we find

$$\partial_t(\rho M_i) + \nabla\cdot(\rho \mathbf{u} M_i) = \mathscr{J}_{M_i} \tag{12}$$

where we define M_i as

$$M_i = \frac{N_i}{\rho} \tag{13}$$

In (12) we also have the right-hand side source term

$$\mathscr{J}_{M_i} = \int_{y_i}^{y_{i+1}} J(s, \mathbf{x}, t)\mathrm{d}s \tag{14}$$

to which we turn next.

In the GDE (8) we conveniently left the source term $J(s, \mathbf{x}, t)$ unspecified for sake of generality. Here, we will consider two main transport mechanisms of droplets, i.e., diffusion due to Brownian motion which is a mechanism of particular relevance for very small droplets in the range of nanometers, and drift due to droplet inertia which is a mechanism dominant for larger droplets in the range of several micrometers. These two mechanisms may be captured in the source term through (Frederix, Kuczaj, et al., 2017):

$$J(s, \mathbf{x}, t) = \nabla\cdot[\mathbb{D}^{\ell}(s)\nabla n(s, \mathbf{x}, t)] - \nabla\cdot[\mathbf{u}^{\ell}(s)n(s, \mathbf{x}, t)] \tag{15}$$

The first term in the right-hand side of this relation represents the droplet diffusivity with size-dependent diffusion coefficient $\mathbb{D}^{\ell}(s)$ for the liquid droplets (hence the superscript ℓ). Moreover, in the second term we introduced a size-dependent drift-velocity $\mathbf{u}^{\ell}$, which is defined such that the droplets move with a velocity $\mathbf{v} = \mathbf{u} + \mathbf{u}^{\ell}$.

To compute the diffusion coefficient $\mathbb{D}^{\ell}(s)$ we adopt the Stokes-Einstein equation, providing a model for the Brownian diffusivity of a spherical body. We implement the formulation as given by Frederix, Kuczaj, et al. (2017) and Hinds (1999), in which the Cunningham correction factor is incorporated to account for surface slip of small droplets. The reader is referred to the work of Frederix, Kuczaj, et al. (2017) and Hinds (1999) for more detail. For the droplet velocity $\mathbf{v}(s)$ we use the 'Full Stokes' model as presented by Frederix, Kuczaj, et al. (2017).

In Eulerian context, the PDE describing the motion of a droplet is given by

$$\partial_t\mathbf{v}(s) + [\mathbf{v}(s)\cdot\nabla]\mathbf{v}(s) = -\frac{1}{\tau}[\mathbf{v}(s) - \mathbf{u}] + (1 - \gamma)\mathbf{g} \tag{16}$$

with the droplet relaxation time

$$\tau = \frac{\rho^{\ell}d^2}{18\mu}, \tag{17}$$

gravitational acceleration $\mathbf{g}$ and density ratio $\gamma = \rho^{v}/\rho^{\ell}$. Eq. (16) can be solved numerically for $\mathbf{v}(s)$. Note that $\mathbf{v}(s) \equiv \mathbf{v}(s, \mathbf{x}, t)$, i.e., a Eulerian velocity field expressing the time-, space- and size-dependent droplet velocity.

2.3. Computing deposition characteristics

When we use a no-slip boundary condition for the mixture velocity $\mathbf{u}$ then $\mathbf{u}$ is zero at the wall. The only two mechanisms allowing for droplet deposition on such walls are then, see Eq. (15), a non-zero drift velocity $\mathbf{u}^{\ell}(s)$, or a non-zero gradient of $n(s, \mathbf{x}, t)$ perpendicular to the wall, i.e., $\nabla n(s, \mathbf{x}, t)\cdot\mathbf{n}$ with $\mathbf{n}$ the general wall normal. We discuss the boundary treatments for both mechanisms next:

1. For the first mechanism the inertial droplet velocity $\mathbf{v}(s)$ must be known at the wall. To numerically do this, a first approach would be to take the wall droplet velocity equal to the velocity of droplets at a computational cell center near the wall if that velocity is wall-ward, as if droplets maintain a constant velocity near the wall. We call this approach the zero-gradient extrapolation model (ZGM) boundary treatment. Alternatively, we may adopt the Lagrangian sub-grid model (LSM) boundary treatment approach proposed by Longest and Oldham (2008) and applied by Frederix, Kuczaj, et al. (2017).
2. The deposition due to diffusion is treated under the assumption of a perfectly absorbing boundary. When droplets hit a wall they are absorbed instantly, and removed from the domain. Diffusional deposition is driven by $\nabla n(s, \mathbf{x}, t)\cdot\mathbf{n}$ being non-zero at the wall. We compute the gradient of M_i at the face *in the diffusion flux* as if M_i is zero at the wall to induce diffusion transport towards the wall. Full details are given by Frederix, Kuczaj, et al. (2017).

In the next Section we specify the numerical methods that have been adopted and show simulation results of flow and deposition in a lung cast.

3. Validation against deposition experiments of the human upper airways

In the previous section the Eulerian aerosol model for droplet deposition by diffusion and drift was presented. In this section, the model will be applied to the prediction of aerosol lung deposition. The main goal of this is to validate the model, as experimental data for regional deposition in a realistic cast of the upper human airways is available. In Section 3.1 the experimental setup is discussed, as well as the experimental conditions at which the lung cast was operated. These conditions must be mimicked accurately, to allow for proper comparison between the numerical and experimental results. The numerical setup is discussed in Section 3.2. Finally, in Section 3.3, we study the deposition rate of aerosol inside the lung cast. Due to the construction of the cast, detailed deposition rates can only be measured per segment experimentally. The per-segment data can also be recovered from the numerical setup. Several simulations will be compared against the experimental data, for different computational grids and comparing the two boundary treatments as outlined in the previous section.

3.1. Experimental setup

Nordlund et al. (2017) presented experiments in a realistic cast of the human upper respiratory tract. In this paper we accurately represent the geometry of this cast numerically, as well as the conditions at which the cast is operated. For completeness, we give a brief overview of the main features of the lung cast.

The lung cast is based on the original model of Lizal et al. (2015). It is a segmented airway model consisting of an oral cavity and subsequent segments down to the seventh generation of lung branching. Fig. 1 (left) shows a visualization of the in silico representation of the human tracheobronchial tree. In the right figure a close-up is shown of the branching geometry as used in the experiment, where it can be clearly seen that the cast is built up of 32 segments, constructed to explicitly distinguish the geometrical features of the airways. The internal geometry of the cast is based on a combination of a digital reference model of the human tracheobronchial tree (Schmidt et al., 2004) and the oral cavity (Cheng, Zhou, & Chen, 1999). The numbering of segments is from top to bottom starting with the oral cavity, as shown in Fig. 1. Segments 23–32 are outlet segments to connect the relatively small seventh generation branches in one larger outlet (see Fig. 1). The flow rate at each of these 10 outlets was set such that the total inlet flow rate is 15 min^{-1}, corresponding to flow conditions in the sedentary regime (Elcner, Lizal, Jedelský, Jícha, & Chovancova, 2016). The outlet flow rates are specified by Nordlund et al. (2017), and correspond to flowrates related to the pneumatic resistance of the model, as reported by Lizal et al. (2015). The maximum Reynolds number inside the cast is approximately 10^3, near the trachea, and much lower in other parts of the lung cast, such that the flow can be regarded as laminar (Nordlund et al., 2017).

Once a steady-state flow is achieved inside the lung cast, an aerosol can be released at the inlet of the mouth. The chosen aerosol was a glycerol-air mixture with a count median aerodynamic diameter of 2.1 μm and a geometric standard deviation of 1.19. This particle size distribution corresponds to the largest sizes which could be reliably created with the aerosol generation method, i.e., a Condensation Monodisperse Aerosol Generator (CMAG) (Nordlund et al., 2017). Fig. 2 shows the experimental droplet size distribution as taken from the work of Nordlund et al. (2017). It can be seen that the highest droplet number concentration is located at 2 μm, while the distribution spans from approximately 1 μm to 4 μm. Also shown in this figure is a log-normal fit to the experimental distribution, with the count median diameter (CMD) set to 2.1 μm and the geometric standard deviation to $\sigma = 1.19$ (Hinds, 1999). Both lines are close to each other and we conclude that a log-normal distribution based on the given CMD and σ represent the experimental droplet size distribution well. In the next subsection we use the mathematically convenient log-normal distribution in our numerical model. It is well known that droplets in the micrometer size range exhibit low Brownian motion as well as modest drift, reducing their deposition efficiency significantly compared to much larger or much smaller droplets. Frederix, Kuczaj, et al. (2017) showed that around $d = 2$ μm the deposition efficiency curve is at a minimum for most Reynolds numbers, in a bent pipe geometry. It was also shown there that numerically, deposition for droplets of these sizes is difficult to predict adequately. This motivates our choice for studying the aerosol dynamics at precisely a droplet size in the micrometer range, as it places a stronger demand on the numerical quality of the simulations and the adopted drift- and diffusion models.

After the lung cast is exposed to the aerosol flow for one hour, the cast can be disassembled into separate segments. The deposited glycerol mass is extracted from each segment by rinsing it with a known amount of 2-propanol solution. Using Gas Chromatography-Mass Spectrometry (GC-MS) the concentration levels of glycerol in the extraction solutions can be measured. The concentration levels are then translated into deposition rates, given the total volume of rinsing solution used and the cast exposure time (1 h). The segments 23–32 are connected to filters and absorb all aerosol droplets which have not deposited inside the cast. These segments, including their filters, are rinsed and measured for glycerol concentration in the same way. Each outlet is connected to a flow controller to be able to set the flow rate through each outlet individually. The sum of all deposited masses of glycerol of all segments is equal to the total mass of glycerol which entered the system.

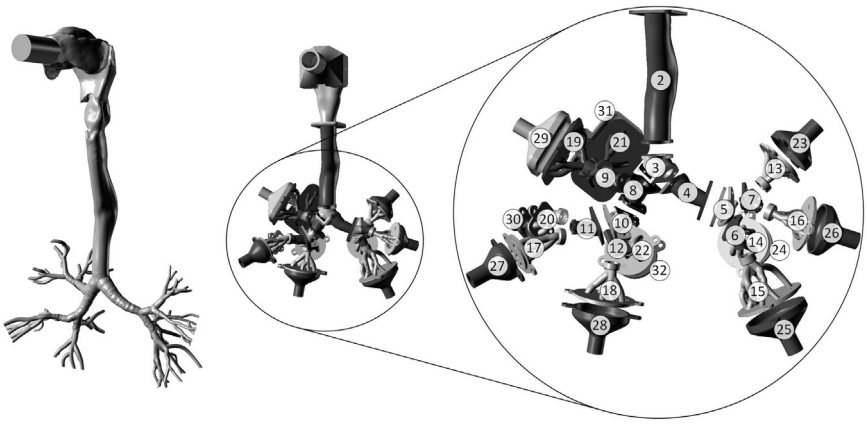

Fig. 1. Left: visualization of the lung cast geometry. Right: visualization of the segmented cast as used in the experiment with segment numbers as indicated (Nordlund et al., 2017).

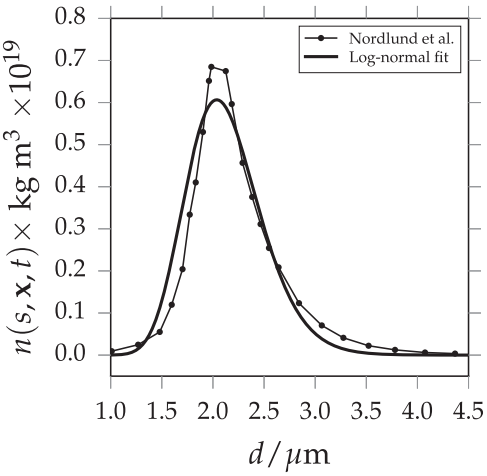

Fig. 2. The glycerol droplet size distribution at the inlet of the cast for the physical experiment (•) (Nordlund et al., 2017) and the numerical simulation (−).

3.2. Numerical setup

Fig. 3 shows the front and side view of the lung cast geometry as used in our simulations. It is a direct copy of the model used for the physical experiments. The inlet, throat, trachea, main bronchi and outlets are shown. As in the physical experiment, the seventh generation is connected to a conically-shaped outlet segments. The inlet and outlets have cylindrical extrusions, such that the flow into and out of the cast may naturally develop without the inlet and outlet condition being of major influence. In order to simulate inside the geometry using a finite volume method, we must create a computational mesh of the geometry. Three computational grids are used to test the mesh dependency of the numerical results. Two meshes (coarse A and fine B) are constructed without boundary layer refinement (-no-bl suffix), and a finer mesh B was constructed also with boundary layer refinement (-bl suffix). On those three distinct meshes simulations are performed using the LSM (-LSM suffix) and ZGM (-ZGM suffix) boundary treatments for the velocity of particles at the wall. Identification of the presented results given a mesh and boundary conditions follows from the syntax which is constructed from the abbreviations (e.g., A-no-bl-LSM to denote results obtained on the coarse grid A, without refinement in the boundary layer close to the wall and with the LSM for the inertial deposition velocity).

In order to determine the necessary cell sizes, Reynolds Averaged Navier-Stokes (RANS) simulations are performed. The commercial StarCCM+ code, version 10.2, is used and the SST k–ω turbulence model is applied. For the determination of the characteristic scales, the resting condition of 15 L/min steady-state flow rate is applied. The bulk computational cell size for the fine mesh B is based on the Taylor scale computed from the RANS simulations (Kuczaj, Komen, & Loginov, 2010). For the boundary layer the non-dimensional wall distance for wall-bounded flows is also computed based on the RANS simulations and the first layer of cells is located at $y^+ = 0.5$, while the last layer has a similar size as the bulk cell size.

The Taylor scale is estimated between 4.5×10^{-4} and 7.5×10^{-4} m, depending on the particular lung regions, while the thickness of the first cell of the triangular prism layer for the selected flow and $y^+ = 0.5$ is found to be 6×10^{-5} m. Depending on the lung region the boundary layer mesh consists of 7–10 cell layers, with thicknesses consecutively growing towards the bulk with a stretching ratio equal to 1.2. For all meshes generated in StarCCM+, the quality of the polyhedral elements is set as high as possible in the software

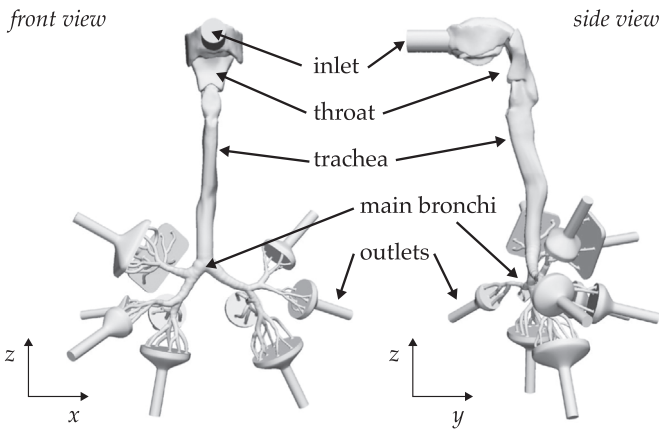

Fig. 3. Front and side view of the lung cast geometry as used in simulations.

setup to obtain a smaller number of cells, and in particular a smaller number of non-orthogonal cells. The mesh A (coarse) was constructed by coarsening the resolution of mesh B with a factor of two. In total, mesh A-no-bl has 583, 088 cells, mesh B-no-bl 1,750,042 cells and mesh B-bl 4,021,078 cells.

Table 1 lists the physical parameters used in the simulations. For the viscosity we use that of air. The liquid density of glycerol is taken from the work of Nordlund et al. (2017). The physical experiment was performed at atmospheric conditions and room temperature. Temperature and pressure changes inside the lung can be assumed to be small such that the system is effectively isothermal. This allows to neglect effects such as condensational growth, evaporation and nucleation, and allows to take the physical parameters listed in Table 1 as constant. In agreement with the experiment the flow rate at the inlet Φ is set to 15 L/min.

Table 2 lists the boundary conditions for the solution variables for the inlet, ten outlets and wall boundary regions. We set the mass fraction of glycerol to a low but arbitrary value of 10^{-5}. Since for such a dilute aerosol there is only one-way coupling (Elghobashi, 1994) (the corresponding volume fraction of glycerol is much smaller than 10^{-5} due to its density) between flow and particulate phase, the concentration of droplets has no effect on the flow or deposition patterns. Also, when discretizing the size space in several sections, these sections do not communicate with each other due to the omitted effects of condensation, evaporation, coagulation, etc, although each representative size s_i associated with a section responds in its own way to the flow. This response depends on the sectional diffusivity $\mathbb{D}_i^\ell \equiv \mathbb{D}^\ell(s_i)$ and sectional droplet velocity $\mathbf{v}_i \equiv \mathbf{v}(s_i)$ consisting of the velocity of the gas mixture $\mathbf{u}$ and the size dependent drift velocities of the droplets. For convenience, we choose to set an arbitrary uniform distribution in sectional space, i.e., $M_i = M_0$ at the inlet. Using the consistency relation (9) it can be derived that $M_0 = Z_{\text{gly}}/\sum_i s_i$ at the inlet, with Z_{gly} the local mass fraction of glycerol. To represent the relevant size space of the glycerol inlet distribution shown in Fig. 2 accurately, we choose $\mathscr{P} = 8$ and a distribution of equally sized sections in d over the domain $d = [1, 4]$ μm. The representative sizes s_i are chosen at the center of each section in d-space. By using the fact that mass fractions sum up to unity, we set the carrier gas mass fraction to $Y_{\text{air}} = 1 - Z_{\text{gly}}$ at the inlet such that droplets are following mixture streamlines. We force the droplet phase at the inlet to have no drift velocity, i.e., $\mathbf{v}_i = \mathbf{u}$ at the inlet. The aerosol enters the cast under atmospheric pressure p_0. We assume that due to the cylindrical outlet extensions as shown in Fig. 3 the flow is sufficiently developed such that a zero-gradient boundary condition can be set for all variables at all outlets. Only the fluid velocity $\mathbf{u}$ is set using a Dirichlet boundary condition. We impose an outward Poiseuille profile with a total flow rate as specified by Nordlund et al. (2017). The sum of all the outlet flow rates equals Φ. For both M_i and Z_{gly} we use the zero-gradient boundary condition when computing the drift flux at the geometry walls and a Dirichlet boundary condition of zero when computing the diffusive flux to mimic a perfectly absorbing surface. No boundary condition is necessary for vapor at the walls because we set the wall vapor flux to zero. For the mixture velocity $\mathbf{u}$ a no-slip condition is applied while we use either the LSM or ZGM boundary treatments for $\mathbf{v}_i$ as will be indicated, at the walls. We start each simulation at $t = 0$ with a quiescent system containing only air at pressure p_0 and temperature T_0. In the time interval $t = [0, 0.1]$ s the outlet velocities are linearly ramped to their values corresponding to a total inlet flow rate of Φ. For the given conditions and meshes all simulations attain a steady state. The results presented in the remainder of this text are taken at $t = 4$ s, a point in time for which all simulations are converged sufficiently to this steady state. We conclude this from the fact that the total flux of droplets leaving the system (via deposition or the outlets) is approximately equal to the total flux of droplets entering the system, to within 5%.

Table 3 shows the numerical schemes used for the various terms in the set of governing equations. For the partial time derivatives we use the θ-scheme (Morton & Mayers, 2005) with $\theta = 0.6$. This gives extra implicit damping and improves convergence to the steady state. We use the 'linear upwind' scheme in the computation of both temperature and velocity at cell faces. This interpolation scheme is a second order upwind-biased scheme and uses the gradient of the velocity to explicitly 'improve' the interpolation from an upwind direction. The Van Leer limiter (van Leer, 1979) is used to interpolate Y_j, Z_j and M_i to cell faces. This combination of schemes for the particular terms performed well in the work of Frederix, Kuczaj, et al. (2017) and is therefore selected here too.

3.3. Deposition efficiency results and comparison

When integrating Eq. (15) over a section and using definition (13) it can be seen that the total sectional number concentration flux at a wall is given by

$$\phi_i = -\rho \mathbf{u}^\ell M_i + \rho \mathbb{D}_i^\ell \nabla M_i, \tag{18}$$

Table 1
Simulation parameters for glycerol droplets carried by air at room temperature and atmospheric conditions. The v superscript denotes a vapor and ℓ a liquid.

Parameter	Value	Unit
μ	1.81×10^{-5}	m^2/s
ρ_{air}^v	1.1898	kg/m^3
ρ_{gly}^ℓ	1258	kg/m^3
T_0	298.15	K
p_0	10^5	Pa
Φ	15	L/min
$\mathbf{g}$	(0, 0, −9.81)	m/s^2

Table 2
Boundary conditions for the given variables and boundary regions. ZG stands for zero-gradient.

Variable	Inlet	Outlets	Walls
Z_{gly}	10^{-5}	ZG	ZG (drift) and 0 (diffusion)
Y_{air}	$1 - Z_{gly}$	ZG	–
M_i	M_0	ZG	ZG (drift) and 0 (diffusion)
T	T_0	ZG	T_0
$\mathbf{u}$	ZG	From Nordlund et al. (2017)	(0, 0, 0) m/s
$\mathbf{v}_i$	$\mathbf{u}$	ZG	LSM or ZGM
p	p_0	ZG	ZG

Table 3
Chosen numerical schemes for the discretization of the indicated terms.

Term	Scheme	Comment
∂_t	θ-scheme (Morton & Mayers, 2005)	All time derivative, $\theta = 0.6$
$\mathbf{u}_f$, T_f	Linear upwind	`linearUpwind linear` in OpenFOAM
$Y_{j,f}$, $Z_{j,f}$, $M_{i,f}$	Van Leer limiter (van Leer, 1979)	`vanLeer` in OpenFOAM
$\mathbf{v}_{i,f}$	Upwind	Provides good convergence
∇ (cell-center gradient)	Central	`linear` in OpenFOAM
∇^2 (Laplacian)	Central corrected	`linear` with non-orth. corr.
∇_f (face-normal gradients)		

which has unit $m^{-2}s^{-1}$, i.e., it gives the section i number of droplets passing per unit area per unit time. Multiplying this by s_i gives the total mass of droplets in section i passing per unit area per unit time, i.e.,

$$\text{flux}_i = \phi_i s_i. \tag{19}$$

The value of flux_i can be computed at the walls of the lung cast, thereby allowing to assess the deposition in different parts of the lung cast.

Fig. 4 shows the deposition patterns in terms of the flux of droplets in section $i = 3$ with size $d = 1.93$ μm close to the value of CMD of the log-normal size distribution as shown in Fig. 2. The lung cast is shown only for segments 1–12 for better visibility of the first bifurcation. The deposition flux is presented for mesh A without boundary layer mesh refinement and mesh B with and without boundary later mesh refinement. The left column shows results using the ZGM deposition velocity boundary treatment and the right column using the LSM. The color represents the flux scaled by the surface-averaged inlet flux. It can be seen that locally the deposition flux exceeds 0.025% of the inlet flux. For the 'no-bl' meshes with the ZGM boundary treatment it is quite difficult to distinguish deposition patterns with a sensible length scale; the deposition appears very pixellated. Moreover, with respect to the other simulations the deposition pattern shows a large overprediction of deposition. This corresponds to the observations made by Frederix, Kuczaj, et al. (2017), where deposition in a bent pipe was studied. When the computational mesh was not refined near the wall of the domain, the ZGM boundary treatment showed large overpredictions of deposition, in particular for droplets in the μm range with flow Reynolds numbers equivalent to the ones in the lung cast ($\mathcal{O}(10^3)$, Nordlund et al., 2017 provided a detailed overview of the per-segment Reynolds numbers). For the 'no-bl' meshes with the LSM treatment, some trends in the deposition pattern become visible – although the deposition is still quite pixellated. For example, a symmetric gradient in deposition flux is shown at the inlet extension (at the mouth). As droplets enter the inlet extension with the same laminar axial velocity as the carrier gas, a non-axial deposition flux there can only be attributed to sedimentation. At the saddle point of the first bifurcation (this point is enlarged in the insets in Fig. 4 for each simulation), an increase of deposition is shown compared to the primary bronchi, which is attributed to inertial impaction due to the large carrier gas velocity and curvature there.

For mesh B with boundary layer mesh refinement the deposition patterns become much smoother and less pixellated, for either boundary treatment scheme. Features of the geometry are now clearly reflected in the deposition patterns. Quite interestingly, the primary bronchi show a 'zebra-like' deposition pattern with rings of local maxima and minima. This deposition pattern appears related to actual anatomical structures in the bronchi walls. After visual inspection we note that the distances between these rings correspond to the length scale of the oscillatory structure of the lung surface, as a result of the tracheal and bronchi rings. Also features in the mouth cavity can be clearly distinguished. Fig. 5 shows the left, right, front and back view of the 'B-bl-ZGM' deposition results for the same droplet size. Here too, features of the geometry can be seen in the pattern of deposition. For example, cavities inside the Larynx are clearly visible due to large deposition there.

After these qualitative considerations, we turn to quantitative comparison against experimental data next. In the physical experiment the total deposition rate R_k in units of μg/hr were measured for each cast segment k. To allow direct comparison of our simulations against this experimental data, we post-process our results in the following way:

1. In the simulations an arbitrary level of inlet concentration was set, i.e., at the inlet the mass fraction for glycerol is $Z_{gly} = 10^{-5}$.

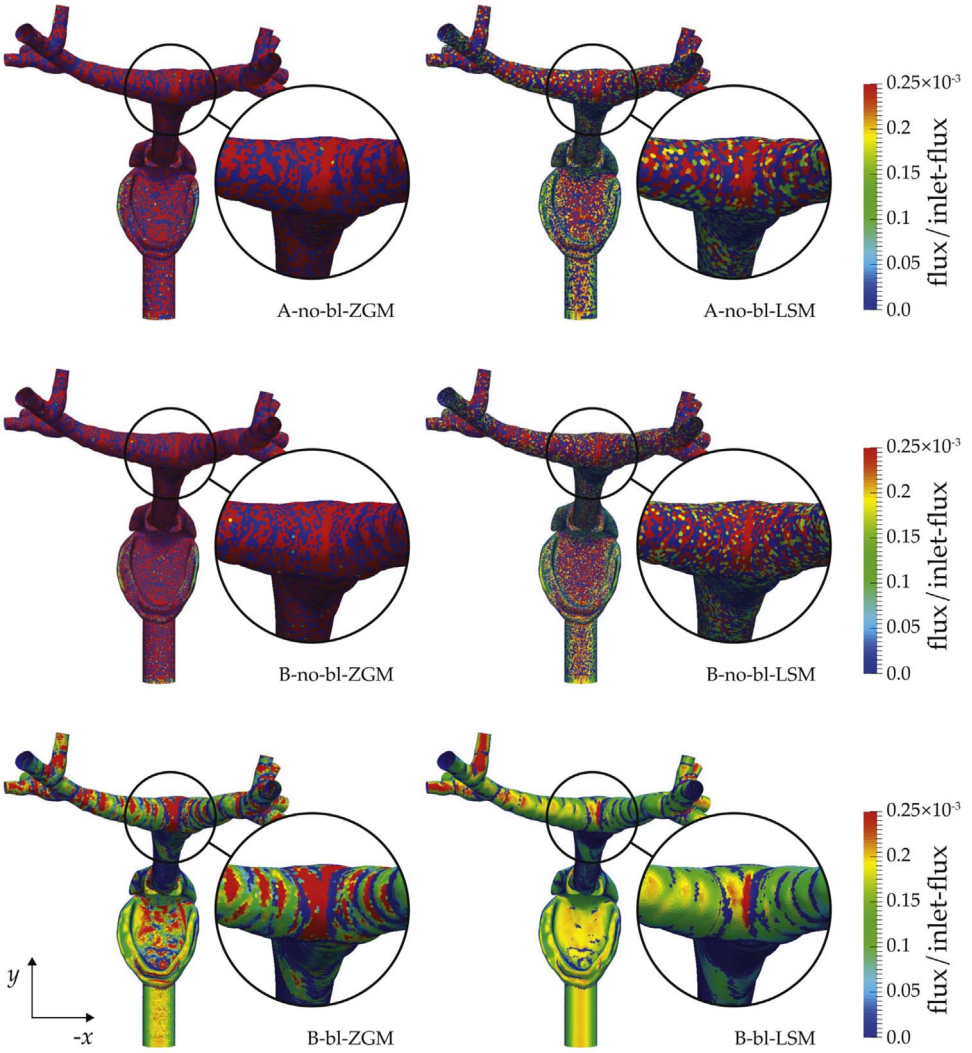

Fig. 4. Deposition fluxes for $d = 1.93$ μm glycerol droplets for the meshes A-no-bl, B-no-bl and B-bl, comparing the LSM and ZGM droplet velocity wall treatments. The color indicates the flux scaled by the surface-averaged inlet flux. The inset shows an enlarged image of the first bifurcation. Only segments 1–12 are shown.

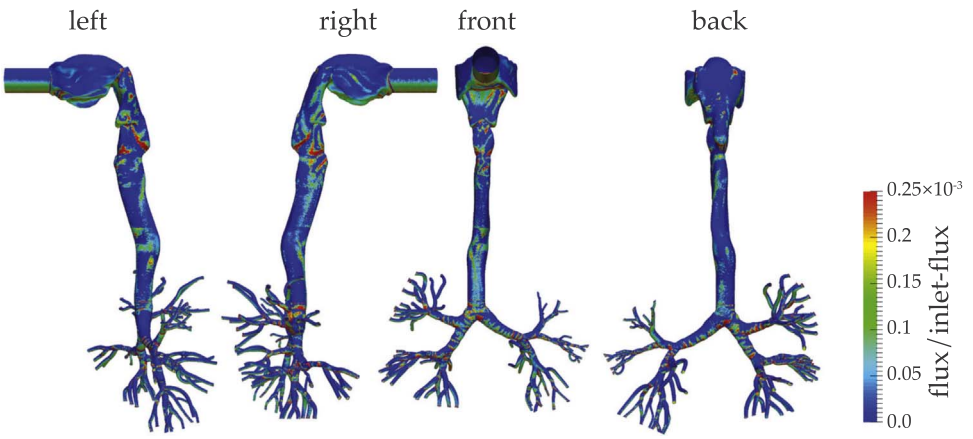

Fig. 5. Left, right, front and back view of the deposition flux for $d = 1.93$ μm glycerol droplets using mesh B with boundary layer mesh refinement at the wall and the ZGM inertial droplet velocity boundary treatment. Segments 1–12 are shown.

This must be accounted for to reflect the experimental inlet concentration. In the experiment all aerosol droplets are either captured by the segments due to deposition, or by the filters at the ten separate outlets. This means that summing all the rates corresponding to all the segments and outlets gives the total influx, from which the experimental $Z_{\text{gly}} = 10^{-5}$ at the inlet can be derived. We scale our deposition rates by the ratio of experimental and numerical $Z_{\text{gly}} = 10^{-5}$.

2. At the inlet we have specified $\mathscr{P} = 8$ sections covering the size domain $d = [1, 4]$ μm in diameter, each with a droplet number concentration of M_0. To accurately mimic the total experimental deposition rate, the sectional deposition fluxes must be scaled by the log-normal size distribution as shown in Fig. 2. We use a weighted average of the sectional fluxes to compute the total per-segment deposition rate

$$R_k = \sum_i w_i \int_{A_k} \text{flux}_i \text{d}A, \tag{20}$$

with A_k the surface area of the k th segment and w_i the weight belonging to the i th section. We let w_i correspond to the surface area underneath a unit log-normal distribution with given CMD and σ corresponding to the part of the size domain for which section i is representative. The i th section covers $[y_i, y_{i+1}]$ in the size domain in terms of mass, and $[d_i, d_{i+1}]$ in terms of diameter. The unit log-normal distribution can be written as (Hinds, 1999):

$$f(d) = \frac{1}{\sqrt{2\pi}\, d \log\sigma} \exp\left(-\frac{(\log d - \log\text{CMD})^2}{2\log^2\sigma}\right). \tag{21}$$

Using σ and CMD as given above, we define the sectional weights as

$$w_i = \int_{d_i}^{d_{i+1}} f(d)\text{d}d. \tag{22}$$

This well-known integral can be expressed using the erf-function. Integrating $f(d)$ from zero to ∞ gives unity. The sum $\sum_i w_i$ represents the integral of $f(d)$ from $d_1 = 1$ μm to $d_{\mathscr{P}+1} = 4$ μm and has a value of 0.99988…, indicating that the relevant size domain of the distribution is captured quite completely with the chosen sections.

With these two post-processing steps completed we can compare the numerical results against the experimental data. Fig. 6 shows both the experimental and numerical data for each cast segment. The numerical data were obtained for six different setups using two meshes, with and without boundary layer grid refinement and the two boundary treatments. For the ZGM boundary treatment (left figure) it is shown that for the adopted spatial resolution and without grid refinement near the wall (i.e.,'-no-bl-ZGM' suffix in the legend) a large overprediction of deposition occurs. In fact, the ratio between R_k for experimental data and 'no-bl-ZGM' numerical data is more than one order of magnitude. The deposition is so large that a significant amount of droplets has already deposited before reaching the outlets, therewith reducing R_k significantly for $k > 22$.

When using the LSM boundary treatment on mesh B with boundary layer grid refinement, the numerical deposition rate agrees well with the experimental data. Given the sensitivity of the experimental data (indicated by the gray area in Fig. 6) it is remarkable how close the numerical predictions are with the measurements. For $13 \leq k \leq 22$ it appears that the 'B-bl-ZGM' results show a small systematic overprediction of the experimental data, although the ratio between R_k for experiment and simulation remains within one decade.

The numerical results using the LSM scheme, see Fig. 6 (right), show for any of the adopted meshes a good agreement with experimental data. These results correspond to the right column of pictures in Fig. 4. It was noted before that the deposition fluxes for

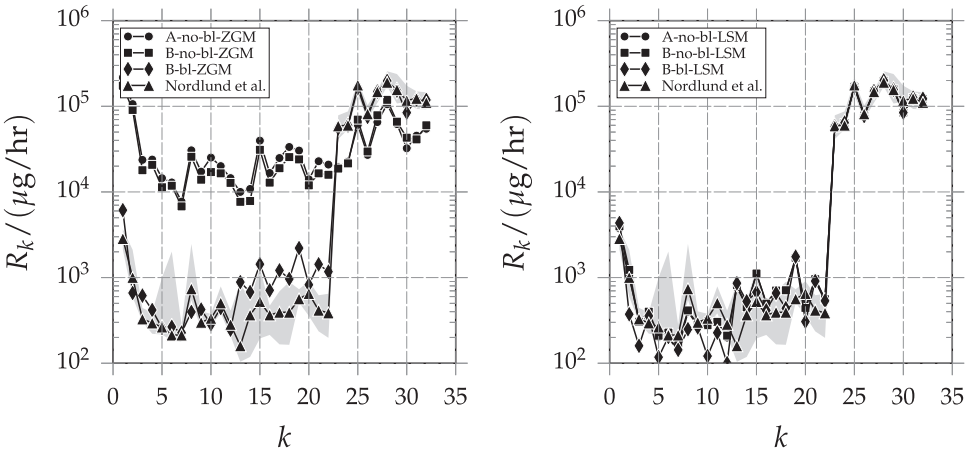

Fig. 6. Per-segment (indexed by k) deposition rates for the simulations and physical experiment as indicated. Left shows the ZGM boundary treatment results and right those for the LSM boundary treatment. Segments 23–32 contain the outlet filters and therefore a large part of the total deposition rate. The gray area marks the range between highest and lowest experimentally measured values, for each k. The points marked as Nordlund et al. are the average of the experimental repetitions.

the 'no-bl' meshes are quite pixellated. Still, the integral quantities R_k for each segment k (they are integral quantities due to the surface integral in Eq. (20)) correspond reasonably well to both the experimental data as well as the predictions for R_k using the wall-refined 'bl' meshes. In practice, the added value of numerical simulation over physical experiment is that local deposition patterns may be accurately resolved instead of only getting regional deposition information as in the experiments. If this is required, then meshes with sufficient resolution near the wall are necessary. Conversely, under-resolved simulations yield correct per-segment deposition rates but this may be more of a coincidence than a numerically reliable simulation feature. In fact, if the most detailed impression of the solution is clearly under-resolved, then any agreement of integral quantities with experiments is rather fortuitous. The results clearly establish that reliable results are achieved at proper spatial resolution and that particularly the resolution of the boundary layer is crucial for high-quality predictions.

To analyze the experimental and numerical results in a more quantitative way, Table 4 shows some of the statistics of both the experimental and numerical work. Since Fig. 6 shows results on a logarithmic scale we have also considered the statistics of the results on this basis. For the experimental results, the per-segment mean μ_k and standard deviation σ_k of the deposition rates are computed as:

$$\mu_k = \text{mean}(\log \mathscr{R}_k) \quad \text{and} \quad \sigma_k = \text{STD}(\log \mathscr{R}_k), \tag{23}$$

with $\mathscr{R}_k$ the set of experimental measurements performed for segment k. We also compute how far numerical result R_k lies from the experimental μ_k with respect to the standard deviation of the experimental results. For this, we introduce C_k, as

$$C_k = \frac{|\mu_k - R_k|}{\sigma_k}, \tag{24}$$

indicating how many STDs the numerical observation is away from the mean experimental observation. The numerical results on the mesh without boundary layer refinement and in cases without the Lagrangian sub-grid model is, averaged over all segments, is found approximately 15 σ_k away from the experimental mean. Adding a boundary layer and/or using LSM is shown to reduce the error with respect to experimental data to about 2 standard deviations.

4. Size-dependent deposition patterns in the human upper airways

In the previous section we have validated our numerical approach against experimental data. We see good agreement for meshes with sufficient resolution near the wall. Also, using the LSM boundary treatment the lack of resolution near the wall can be partially compensated by adopting a Lagrangian sub-grid model. In this section we extend the previous simulations by increasing the size domain and number of sections such that both the diffusional and inertial deposition regimes (Frederix, Kuczaj, et al., 2017) are represented. The main intention of this is to illustrate the capabilities of our method. The validity of the results is underlined by 1) the experimental agreement with deposition data for the real geometry as seen in the previous section in the micrometer size range and

Table 4
Per segment mean (μ_k) and standard deviation (σ_k) of the logarithm of the deposition rate R_k for the experiment (second column). Also the numerical data is shown for B-no-bl-ZGM, B-bl-ZGM and B-no-bl-LSM, with C_k a measure for how far the numerical observation is away from the experimental mean, see Eq. (24).

	Nordlund et al.	**No BL & no LSM**		**With BL**		**With LSM**	
k	$\mu_k \pm \sigma_k$	$\log R_k$	C_k	$\log R_k$	C_k	$\log R_k$	C_k
1	3.44942 ± 0.0799839	5.23986	22.385	3.78684	4.21866	3.59826	1.86085
2	3.01271 ± 0.160937	4.95702	12.0812	2.82028	1.19572	3.08958	0.477611
3	2.54226 ± 0.0611047	4.25388	28.0113	2.78925	4.04218	2.48355	0.960744
4	2.47118 ± 0.073188	4.31604	25.2071	2.6213	2.05115	2.60136	1.77864
5	2.49681 ± 0.20742	4.05492	7.51186	2.41183	0.409698	2.3205	0.850038
6	2.45542 ± 0.323682	4.07236	4.99548	2.42456	0.095346	2.35753	0.302416
7	2.33273 ± 0.0530852	3.83144	28.2321	2.35649	0.447581	2.23371	1.86536
8	2.94188 ± 0.231113	4.41055	6.35474	2.59816	1.48725	2.61679	1.40665
9	2.4764 ± 0.0601194	4.14268	27.7162	2.62656	2.49779	2.45208	0.404538
10	2.5085 ± 0.0571888	4.23197	30.1365	2.45552	0.92644	2.44426	1.12317
11	2.69536 ± 0.0941775	4.21752	16.1627	2.64383	0.547192	2.48293	2.25563
12	2.48387 ± 0.0933735	4.10556	17.3678	2.39242	0.979432	2.32206	1.73295
13	2.33223 ± 0.311387	3.88422	4.98411	2.94698	1.97421	2.91435	1.86942
14	2.47042 ± 0.231962	3.89425	6.13822	2.8308	1.55362	2.65332	0.788503
15	2.69139 ± 0.247516	4.49181	7.27394	3.15588	1.87658	3.04753	1.43886
16	2.54024 ± 0.118385	4.10871	13.249	2.85127	2.62727	2.69577	1.31376
17	2.57813 ± 0.18435	4.27734	9.21732	3.08367	2.74229	2.84792	1.46345
18	2.55804 ± 0.277764	4.40696	6.65641	2.98411	1.53393	2.85235	1.05954
19	2.76768 ± 0.0522813	4.38006	30.8404	3.34429	11.0289	3.23116	8.86518
20	2.76642 ± 0.142713	4.07718	9.18463	2.91623	1.04974	2.64594	0.84421
21	2.61889 ± 0.13163	4.2174	12.1439	3.1547	4.07056	2.98149	2.75466
22	2.55343 ± 0.20572	4.20013	8.0046	3.06919	2.5071	2.7464	0.93804
Average over k:			15.1752		2.26648		1.65246

2) the agreement of the model for a much larger size range with literature available for a bent-pipe geometry (Frederix, Kuczaj, et al., 2017). We do this using the 'B-bl-LSM' setup, i.e., mesh B with boundary layer refinement and the LSM boundary treatment for the deposition velocity. This setup was shown to give accurate results in comparison with the experimental lung cast data, while producing visually smooth deposition flux fields.

We set the number of sections to $\mathscr{P} = 16$ using an equidistant sectional distribution in $\log d$-space spanning $d \in [10^{-2}, 20]$ μm, with the representative sizes halfway each section in $\log d$-space. For these sizes, based on the work by Frederix, Kuczaj, et al. (2017), we expect that both the diffusional and inertial deposition regimes are included. All initial and boundary conditions remain equal to those used in the previous section. Using the sectional consistency relation we set one sectional droplet number concentration equal to $M_i = Z_{\text{gly}}/\sum_i s_i$ for all sections at the inlet.

We study quantitatively the deposition behavior inside the lung cast, as a function of droplet size. To that end, we introduce the following quantity:

$$\eta_g(s_i) = -\frac{\int_{A_g} \text{flux}_i \text{d}A}{\int_{A_{\text{inlet}}} \text{flux}_{\text{inlet}} \text{d}A}, \tag{25}$$

representing the per-generation deposition efficiency of droplets of size s_i, for lung structures of generation g, with A_g the wall surface of all segments belonging to generation g. The 'connectivity' between cast segment k and lung generation g is explained by Nordlund et al. (2017), where a detailed table indicates to which generation g part k belongs. The numerator of (25) denotes the total number of droplets in section i depositing on the wall of the g th generation of the lung cast, per unit of time. The denominator denotes the total flux of droplets in section i that enters through the inlet. As this has a negative sign, the definition of η_g contains a minus sign. In short, η_g gives the mass deposition rate of droplets of size s_i into the lung cast wall belonging to generation g with respect to the inflow rate.

Fig. 7 (left) shows η_g in a bar diagram for the different groups of lung generations. The experimental lung cast is constructed such that segments $k > 12$ contain multiple lung generations. These segments are grouped together. Clearly, a 'V-shaped' deposition efficiency is shown, with approximately $d \approx 0.8$ μm separating the predominantly diffusional regime from the predominantly inertial regime. This also shows that the glycerol distribution as used in the previous Section with CMD = 2.1 is close to the minimum of the V-curve, indicating that diffusional and inertial deposition are both relevant deposition mechanisms. For the section representing the largest droplets, the total efficiency of the lung cast is close to unity; almost all droplets have deposited, leaving no chance for droplets to escape through the outlets. In Fig. 7 (right) the partitioning of deposition in the various size classes and generation of lung structures is shown. Of the total mass which deposits per unit of time, the colors indicate what percentage of those droplets deposit in which generation of the lung. It can be seen that approximately half of the droplets deposit in the throat and generations 0–3. The other half deposits in generations 4–7. Only for the section containing the largest droplets, most droplets deposit early on in the lung cast. In fact, approximately 50% of the droplets entering the mouth deposit inside the throat. The partitioning of deposition with respect to the lung generation is reasonably uniform in the size domain for $d < 0.4$ μm, i.e., the diffusional deposition regime. In the inertial regime the partitioning of deposition depends on size. For example, the throat has an enhanced deposition with respect to the total deposition for approximately $0.4 < d < 2$ μm. For $2 < d < 10$ μm the percentage of deposition in the throat decreases and for $d > 10$ μm a rapid increase occurs. This is the result of a complex geometry-dependent interplay of droplet inertia, drag and gravity. Droplet diffusivity is negligible for these droplet diameters.

The per-generation deposition efficiency η_g is proportional to the number of droplets depositing inside the parts of the cast belonging to generation g. In some respect, this could be misleading, since some generations may be very efficient in capturing droplets but have only a small amount of surface area to capture these droplets. To assess the efficiency with which each lung

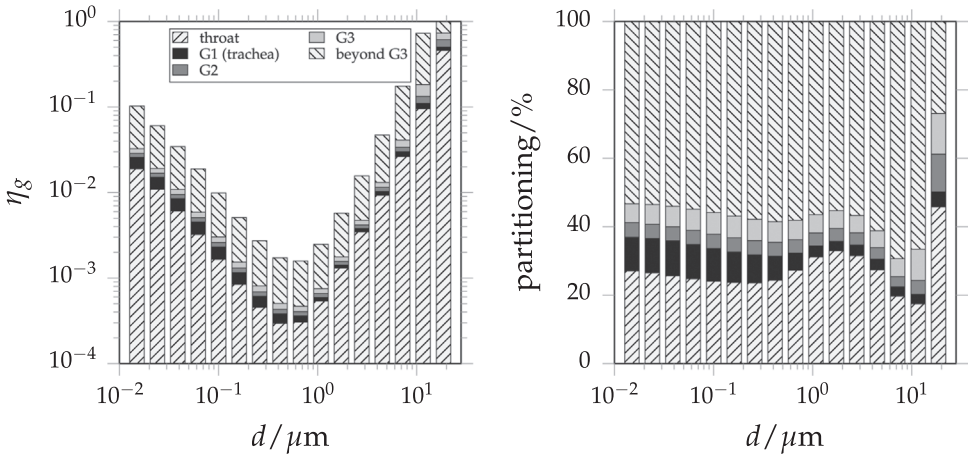

Fig. 7. Per-generation deposition efficiency η_g (left) and the per-generation partitioning of the deposition efficiency (right). For $k > 12$ the segments include multiple generations, and are grouped together with segments which contain the same generations (Nordlund et al., 2017). Each segment is counted only once.

generation captures droplets independent of its amount of lung tissue surface area, we may alternatively have a look at a per-generation average of flux_i, indicating more objectively the deposition efficiency of a lung generation as a function of size. Note, however, that inevitably higher generations receive fewer droplets due to the fact that they have already deposited in earlier generations, reducing the flux. We define the per-generation surface-averaged deposition efficiency as

$$\epsilon_g(s_i) = -\frac{A_{\text{inlet}} \int_{A_g} \text{flux}_i \mathrm{d}A}{A_g \int_{A_{\text{inlet}}} \text{flux}_i \mathrm{d}A} = \frac{A_{\text{inlet}}}{A_g}\eta(s_i). \tag{26}$$

This quantity is shown in Fig. 8. In this figure generations 4–7 were grouped together, as the segments constituting these generations sometimes contain multiple generations making it difficult to analyze deposition inside one of these generations alone. It can be seen in Fig. 8 that the largest surface-averaged deposition efficiency is G3, for all droplet sizes shown. This generation consists of segments 5 and 8 of the lung cast, i.e., the second bifurcation, after the main bronchi. In the inertial regime for approximately $d > 0.4$ μm the surface-averaged efficiency of G1 (i.e., segment 2, trachea) is always much smaller than the other deposition efficiencies. This is because segment 2 resembles closely a vertically placed pipe. Due to gravity larger droplets fall through this pipe without having a large probability of colliding with a wall. Only for the last section shown in Fig. 8 the group G4–G7 has the smallest surface-averaged efficiency with respect to the other groups. This is because deposition in earlier generations is so significant that only a drastically reduced number of droplets reaches these later generations, reducing deposition there. This is in agreement with the data shown in Fig. 8.

5. Conclusions

Size-dependent aerosol deposition in a realistic cast of the human upper airways was studied using an Eulerian internally mixed multi-species aerosol model (Frederix, Kuczaj, et al., 2017), in which the size distribution was discretized using a sectional method. This allowed to capture size-dependent aerosol dynamics such as inertial aerosol drift, gravitational settling and droplet diffusion, accurately and without prior assumptions on the shape or moments of the droplet size distribution. The model was derived by Frederix, Kuczaj, et al. (2017), and an overview of the most important aspects was given in the current paper.

We compared predictions of our model against the experimental data of Nordlund et al. (2017) for regional droplet deposition. We introduced two treatments for the numerical computation of the inertial droplet velocity at the wall: a simple zero-gradient extrapolation model and a Lagrangian sub-grid model (Longest & Oldham, 2008). When looking at the deposition rate integrated over the surface area of a segment of the cast (e.g., the throat, trachea and first bifurcation form one segment), the use of the ZGM boundary treatment results in an overprediction of more than one order of magnitude while with LSM the overprediction significantly reduces and agrees well with the experimental data on any of the adopted meshes. Nevertheless, if the detailed deposition patterns are under-resolved for either boundary treatment a rather pixellated prediction of deposition patterns is found. Agreement of integral quantities with experimental data, as observed with LSM even on coarse meshes, could be somewhat fortuitous. Reliable results are achieved only at proper spatial resolution, where in particular the resolution of the boundary layer is crucial.

Finally, we studied size-dependent aerosol deposition inside the lung cast by exposing it to a polydisperse aerosol spanning a large size range from 10 nm to 20 μm. We presented the partitioning of the total deposition for each generation, and quantified the size-dependent deposition also for droplets that penetrate deeper into the lung. For large droplets we saw that most deposition took place inside the throat. The deposition of small droplets in the diffusional side of the size domain was much more uniform across the various generations of lung structures.

We also studied the surface-averaged deposition efficiency for each generation of the lung. This quantity captures the deposition rate, and reports how well a particular airway generation captures droplets independent of the surface area of the lung generation. We showed that the second generation of the lung tree, i.e., the bifurcation of the main bronchi, has the largest surface-averaged efficiency. For small droplet sizes the throat is much less effective in capturing droplets than other generations of the lung tree,

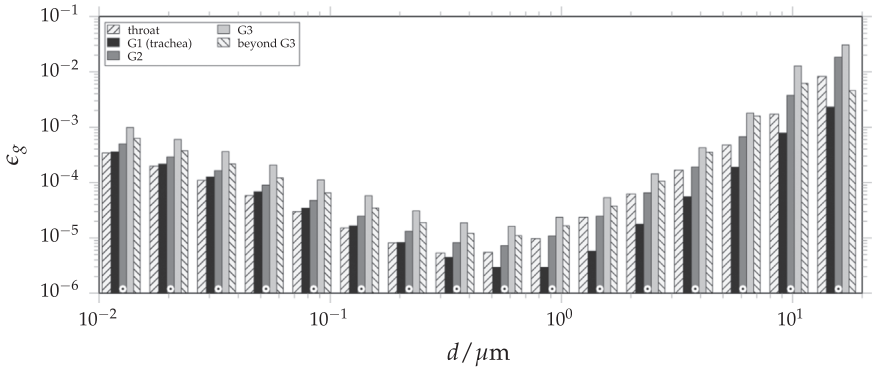

Fig. 8. The per-generation surface-averaged deposition flux efficiency, per section. The colors are associated with different generations of the lung (as indicated), where all lung cast segments belonging to generation 4 or higher are grouped together.

whereas for large sizes the throat's efficiency increases due to inertial droplet motion.

This paper demonstrated the successful application of the sectional compressible Eulerian aerosol model inside complex geometries. This model, unique in its consistent formulation and allowing to embed well-known constitutive thermophysical laws for the description of the mixture, remained computationally feasible for the adopted meshes and sectional discretization. Rich aerosol physics were introduced in the model, allowing for a non-trivial development of an initial size distribution due to size-dependent inertial droplet drift, gravitational settling, diffusion and eventual deposition.

Acknowledgements

- The research presented in this work was funded by Philip Morris Products S.A. (part of Philip Morris International group of companies).
- The authors would like to thank Arne Siccama (NRG) for development and generation of the computational meshes.
- The team from Brno University of Technology was supported by the Czech Grant Agency project 'GA16-23675S' and Brno University of Technology project 'FSI-S-14-2355'.

References

Alzahrany, M., & Banerjee, A. (2015). Aerosolized drug delivery in patient-specific lung model during invasive high frequency oscillatory ventilation. *Journal of Aerosol Science, 81*, 1–20.

Bird, B., Stewart, W., & Lightfoot, E. (2007). *Transport phenomena* (2nd ed.). John Wiley & Sons, Inc.

Cheng, Y., Zhou, Y., & Chen, B. (1999). Particle deposition in a cast of human oral airways. *Aerosol Science & Technology, 31*, 286–300.

Elcner, J., Lizal, F., Jedelský, J., Jícha, M., & Chovancova, M. (2016). Numerical investigation of inspiratory airflow in a realistic model of the human tracheobronchial airways and a comparison with experimental results. *Biomechanics and Modeling in Mechanobiology, 15*, 447–469.

Elghobashi, S. (1994). On predicting particle-laden turbulent flows. *Applied Scientific Research, 52*, 309–329.

Feng, Y., & Kleinstreuer, C. (2014). Micron-particle transport, interactions and deposition in triple lung-airway bifurcations using a novel modeling approach. *Journal of Aerosol Science, 71*, 1–15.

Feng, Y., Kleinstreuer, C., Castro, N., & Rostami, A. (2016). Computational transport, phase change and deposition analysis of inhaled multicomponent droplet–vapor mixtures in an idealized human upper lung model. *Journal of Aerosol Science, 96*, 96–123.

Frederix, E., Kuczaj, A., Nordlund, M., Veldman, A., & Geurts, B. (2017a). Eulerian modeling of inertial and diffusional aerosol deposition in bent pipes. *Computers & Fluids*. http://dx.doi.org/10.1016/j.compfluid.2017.09.018 (in press).

Frederix, E., Stanic, M., Kuczaj, A., Nordlund, M., & Geurts, B. (2016). Characteristics-based sectional modeling of aerosol nucleation and condensation. *Journal of Computational Physics, 326*, 499–515.

Frederix, E., Stanic, M., Kuczaj, A., Nordlund, M., Veldman, A., & Geurts, B. (2017b). Application of the characteristics-based sectional method to spatially varying aerosol formation and transport. *Journal of Aerosol Science, 104*, 123–140.

Friedlander, S. (2000). *Smoke, dust, and haze: Fundamentals of aerosol dynamics* (2nd ed.). Oxford University Press.

Friedlander, S. K. (1983). Dynamics of aerosol formation by chemical reaction. *Annals of the New York Academy of Sciences, 404*, 354–364.

Gelbard, F., Fitzgerald, J., & Hoppel, W. (1998). A one-dimensional sectional model to simulate multicomponent aerosol dynamics in the marine boundary layer: 3. Numerical methods and comparisons with exact solutions. *Journal of Geophysical Research: Atmospheres, 103*, 16119–16132.

Gelbard, F., Tambour, Y., & Seinfeld, J. (1980). Sectional representations for simulating aerosol dynamics. *Journal of Colloid and Interface Science, 76*, 541–556.

Hinds, W. (1999). *Aerosol technology* (2nd ed.). John Wiley & Sons, Inc.

Hofmann, W. (2011). Modelling inhaled particle deposition in the human lung-a review. *Journal of Aerosol Science, 42*, 693–724.

Holbrook, L., & Worth Longest, P. (2013). Validating CFD predictions of highly localized aerosol deposition in airway models: In vitro data and effects of surface properties. *Journal of Aerosol Science, 59*, 6–21.

Hounslow, M., Ryall, R., & Marshall, V. (1988). A discretized population balance for nucleation, growth, and aggregation. *AIChE Journal, 34*, 1821–1832.

Krause, F., Wenk, A., Lacor, C., Kreyling, W., Moeller, W., & Verbanck, S. (2013). Numerical and experimental study on the deposition of nanoparticles in an extrathoracic oral airway model. *Journal of Aerosol Science, 57*, 131–143.

Kuczaj, A., Komen, E., & Loginov, M. (2010). Large Eddy Simulation study of turbulent mixing in a T-junction. *Nuclear Engineering and Design, 240*, 2116–2122.

Kumar, S., & Ramkrishna, D. (1996). On the solution of population balance equations by discretization-I. A fixed pivot technique. *Chemical Engineering Science, 51*, 1311–1332.

Kundu, P., & Cohen, I. (2008). *Fluid mechanics.* Academic Press.

van Leer, B. (1979). Towards the ultimate conservative difference scheme. V. A second-order sequel to Godunov's method. *Journal of Computational Physics, 32*, 101–136.

Li, Z., Kleinstreuer, C., & Zhang, Z. (2007). Particle deposition in the human tracheobronchial airways due to transient inspiratory flow patterns. *Journal of Aerosol Science, 38*, 625–644.

Lizal, F., Bělka, M., Adam, J., Jedelský, J., & Jícha, M. (2015). A method for in vitro regional aerosol deposition measurement in a model of the human tracheobronchial tree by the positron emission tomography. *Proceedings of the Institution of Mechanical Engineers, Part H: Journal of Engineering in Medicine, 229*, 750–757.

Longest, P. W., & Oldham, M. (2008). Numerical and experimental deposition of fine respiratory aerosols: Development of a two-phase drift flux model with near-wall velocity corrections. *Journal of Aerosol Science, 39*, 48–70.

Ma, B., Ruwet, V., Corieri, P., Theunissen, R., Riethmuller, M., & Darquenne, C. (2009). CFD simulation and experimental validation of fluid flow and particle transport in a model of alveolated airways. *Journal of Aerosol Science, 40*, 403–414.

Mitsakou, C., Helmis, C., & Housiadas, C. (2005). Eulerian modelling of lung deposition with sectional representation of aerosol dynamics. *Journal of Aerosol Science, 36*, 75–94.

Morton, K., & Mayers, D. (2005). *Numerical solution of partial differential equations.* Cambridge University Press.

Nordlund, M., Bělka, M., Kuczaj, A., Lizal, F., Jedelský, J., Elcner, J., ... Hoeng, J. (2017). Multicomponent aerosol particle deposition in a realistic cast of the human upper respiratory tract. *Inhalation Toxicology, 29*, 113–125.

Schmidt, A., Zidowitz, S., Kriete, A., Denhard, T., Krass, S., & Peitgen, H. (2004). A digital reference model of the human bronchial tree. *Computerized Medical Imaging and Graphics, 28*, 203–211.

Schroeter, J., Asgharian, B., Price, O., Kimbell, J., Kromidas, L., & Singal, M. (2016). Simulation of the phase change and deposition of inhaled semi-volatile liquid droplets in the nasal passages of rats and humans. *Journal of Aerosol Science,* 95.

Varghese, S., & Gangamma, S. (2009). Particle deposition in human respiratory system: Deposition of concentrated hygroscopic aerosols. *Inhalation Toxicology, 21*, 619–630.

Wexler, A., & Park, S. (2008). Size-dependent deposition of particles in the human lung at steady-state breathing. *Journal of Aerosol Science, 39*, 266–276.

Worth Longest, P., & Oldham, M. (2006). Mutual enhancements of CFD modeling and experimental data: A case study of 1-μm particle deposition in a branching airway model. *Inhalation Toxicology, 18*, 761–771.

Worth Longest, P., & Xi, J. (2007). Effectiveness of direct lagrangian tracking models for simulating nanoparticle deposition in the upper airways. *Aerosol Science and Technology, 41*, 380–397.
Xi, J., & Longest, P. (2009). Characterization of submicrometer aerosol deposition in extrathoracic airways during nasal exhalation. *Aerosol Science and Technology, 43*, 808–827.
Zhang, Z., Kim, C., & Kleinstreuer, C. (2006). Water vapor transport and its effects on the deposition of hygroscopic droplets in a human upper airway model. *Aerosol Science and Technology, 40*, 1–16.
Zhang, Z., Kleinstreuer, C., & Hyun, S. (2012). Size-change and deposition of conventional and composite cigarette smoke particles during inhalation in a subject-specific airway model. *Journal of Aerosol Science, 46*, 34–52.
Zhang, Z., Kleinstreuer, C., & Kim, C. (2009). Comparison of analytical and CFD models with regard to micron particle deposition in a human 16-generation tracheobronchial airway model. *Journal of Aerosol Science, 40*, 16–28.
Zhang, Z., Kleinstreuer, C., Kim, C., & Cheng, Y. (2004). Vaporizing microdroplet inhalation, transport, and deposition in a human upper airway model. *Aerosol Science and Technology, 38*, 36–49.